AGU PUBLICATIONS

JGR

Journal of Geophysical Research: Space Physics

RESEARCH ARTICLE

10.1002/2014JA019849

Key Points:
- Lunar tide is important for simulating ionosphere during the 2009 SSW
- Electric field changes are primary cause of electron density variability
- Meridional winds and thermosphere composition also influence electron density

Correspondence to:
N. M. Pedatella,
nickp@ucar.edu

Citation:
Pedatella, N. M., H.-L. Liu, F. Sassi, J. Lei, J. L. Chau, and X. Zhang (2014), Ionosphere variability during the 2009 SSW: Influence of the lunar semidiurnal tide and mechanisms producing electron density variability, *J. Geophys. Res. Space Physics*, *119*, 3828–3843, doi:10.1002/2014JA019849.

Received 10 FEB 2014
Accepted 16 APR 2014
Accepted article online 23 APR 2014
Published online 7 MAY 2014

Ionosphere variability during the 2009 SSW: Influence of the lunar semidiurnal tide and mechanisms producing electron density variability

N. M. Pedatella[1], H.-L. Liu[2], F. Sassi[3], J. Lei[4], J. L. Chau[5], and X. Zhang[6]

[1]COSMIC Program Office, University Corporation for Atmospheric Research, Boulder, Colorado, USA, [2]High Altitude Observatory, National Center for Atmospheric Research, Boulder, Colorado, USA, [3]Space Science Division, Naval Research Laboratory, Washington, District of Columbia, USA, [4]CAS Key Laboratory of Geospace Environment, Department of Geophysics and Planetary Sciences, University of Science and Technology of China, Hefei, China, [5]Leibniz Institute of Atmospheric Physics, Rostock University, Kühlungsborn, Germany, [6]Department of Aerospace Engineering Sciences, University of Colorado Boulder, Boulder, Colorado, USA

Abstract To investigate ionosphere variability during the 2009 sudden stratosphere warming (SSW), we present simulation results that combine the Whole Atmosphere Community Climate Model Extended version and the thermosphere-ionosphere-mesosphere electrodynamics general circulation model (TIME-GCM). The simulations reveal notable enhancements in both the migrating semidiurnal solar (*SW*2) and lunar (M_2) tides during the SSW. The *SW*2 and M_2 amplitudes reach ~50 m s^{-1} and ~40 m s^{-1}, respectively, in zonal wind at *E* region altitudes. The dramatic increase in the M_2 at these altitudes influences the dynamo generation of electric fields, and the importance of the M_2 on the ionosphere variability during the 2009 SSW is demonstrated by comparing simulations with and without the M_2. TIME-GCM simulations that incorporate the M_2 are found to be in good agreement with Jicamarca Incoherent Scatter Radar vertical plasma drifts and Constellation Observing System for Meteorology, Ionosphere, and Climate (COSMIC) observations of the maximum *F* region electron density. The agreement with observations is worse if the M_2 is not included in the simulation, demonstrating that the lunar tide is an important contributor to the ionosphere variability during the 2009 SSW. We additionally investigate sources of the *F* region electron density variability during the SSW. The primary driver of the electron density variability is changes in electric fields. Changes in meridional neutral winds and thermosphere composition are found to also contribute to the electron density variability during the 2009 SSW. The electron density variability for the 2009 SSW is therefore not solely due to variability in electric fields as previously thought.

1. Introduction

The high-latitude wintertime stratosphere is frequently disturbed due to the interaction between upward propagating waves and the zonal mean flow. In the most dynamically disturbed cases, referred to as sudden stratosphere warmings (SSWs), the stratospheric polar temperature rapidly increases, the normally eastward winds in the high-latitude stratosphere (60°N and 10 hPa) decelerate, potentially reversing direction, and the structure of the polar vortex changes significantly [*Schoeberl*, 1978; *Harvey et al.*, 2002; *Limpasuvan et al.*, 2004; *Charlton and Polvani*, 2007]. A SSW is considered to be a major warming if the zonal mean zonal wind at 60°N and 10 hPa reverses from eastward to westward. During minor SSWs, the zonal mean zonal wind at 60°N and 10 hPa decelerates but remains eastward. Several studies have demonstrated that significant cooling occurs in the mesosphere and lower thermosphere (MLT) during SSWs [e.g., *Walterscheid et al.*, 2000; *Liu and Roble*, 2002; *Hoffmann et al.*, 2007; *Manney et al.*, 2008, 2009], and the effects of SSWs are thus not limited to the high-latitude stratosphere but rather extend throughout the atmosphere.

A connection between variability in the stratosphere and the ionosphere was first recognized several decades ago [*Fraser and Thorpe*, 1976; *Fraser and Wratt*, 1976; *Fraser*, 1977]. *Stening* [1977] and *Stening et al.* [1996] were the first to hypothesize a connection between SSWs and variability in the low-latitude ionosphere. Despite these early studies, it is only recently that the coupling between SSWs and ionosphere variability has been investigated in significant detail. This is likely related to an increased appreciation for the role of the lower atmosphere on producing ionosphere variability, along with the increasing number of global observations. More recent observations have demonstrated the impact of SSWs on equatorial vertical

plasma drifts [*Chau et al.*, 2009, 2010; *Fejer et al.*, 2010, 2011; *Rodrigues et al.*, 2011], geomagnetic observations [*Yamazaki et al.*, 2012a, 2012b], ionosphere electron densities [*Goncharenko et al.*, 2010a, 2010b; *Lin et al.*, 2012; *Pancheva and Mukhtarov*, 2011; *Yue et al.*, 2010], and ion temperatures [*Goncharenko and Zhang*, 2008]. The ionosphere variability during SSWs has also been simulated by coupling whole atmosphere models with global models of the ionosphere [*Fuller-Rowell et al.*, 2010, 2011; *Jin et al.*, 2012; *Pedatella and Liu*, 2013]. Numerical simulations clearly demonstrate that the changes in the ionosphere during SSWs are driven by the upward propagation of dynamical variability from the lower atmosphere and not of external (i.e., solar) origin.

Although the connection between SSWs and ionosphere variability is now well established observationally, the mechanisms responsible for generating the ionosphere disturbances remains an active area of research. The generally accepted mechanism for coupling SSWs to ionosphere variability is through modulation of solar and/or lunar atmospheric tides [*Chau et al.*, 2012]. In particular, changes in the solar and lunar migrating semidiurnal tides (*SW*2 and M_2, respectively), and the westward propagating nonmigrating semidiurnal tide with zonal wave number 1 (*SW*1) are thought to be responsible for generating the ionosphere variability. Changes in the migrating diurnal tide (*DW*1) may also occur during SSWs. Compared to the in situ component generated by solar radiation, the upward propagating component of the *DW*1 does not significantly influence the electrodynamics [e.g., *Millward et al.*, 2001], and SSW-induced variability in the upward propagating *DW*1 is therefore not thought to have a large impact on the ionosphere. The tidal variability can influence the dynamo generation of electric fields and subsequently generate changes in ionospheric electron densities [e.g., *Liu and Richmond*, 2013]. Tidal changes during SSWs may occur due to the influence of changes in the zonal mean atmosphere on tidal propagation [*Stening et al.*, 1997; *Jin et al.*, 2012; *Forbes and Zhang*, 2012; *Pedatella and Liu*, 2013], changes in ozone forcing of the *SW*2 [*Goncharenko et al.*, 2012], and nonlinear planetary wave tide interactions [*Pedatella and Forbes*, 2010; *Liu et al.*, 2010]. Using idealized simulations, *Pedatella and Liu* [2013] concluded that, for an average major SSW, the ionosphere variability is primarily due to the *SW*2, with secondary contributions from the *SW*1 and M_2. The ionosphere variability during SSWs is thus connected to changes in several different atmospheric tides.

In addition to changes in electric fields, other mechanisms have the potential to produce electron density variability during SSWs. Observations of *Gong et al.* [2013] reveal changes in the meridional winds at *F* region altitudes during SSWs. Furthermore, *Goncharenko et al.* [2013] observed significant tidal variability in ion temperature at *F* region altitudes, and the tides in *F* region winds are also likely to be modulated during SSWs. *F* region meridional winds are a well-known mechanism for changing the *F* region peak height (HmF2) and electron density [e.g., *Rishbeth*, 1967]. Changes in *F* region meridional winds should therefore be considered a possible contributor to the ionosphere variability during SSWs. Another potential mechanism for generating ionosphere variability during SSWs is changes in O/N_2. O^+ is the dominant ion in the *F* region, and it is primarily produced by photo-ionization of O. Loss of O^+ occurs through ion exchange reactions with O_2 and N_2 and subsequent dissociative recombination [e.g., *Rishbeth*, 1962]. Changes in O/N_2 thus influence the production and loss of O^+ ions, leading to changes in the electron density. Dissipation of tides influences O/N_2 through changes in the global thermospheric circulation [*Forbes et al.*, 1993; *Yamazaki and Richmond*, 2013; *Siskind et al.*, 2014], and given that large tidal changes are known to occur during SSWs, it is therefore considered plausible that O/N_2 variability may play a role in generating ionospheric variability during SSWs.

In the present study, a combination of the National Center for Atmospheric Research (NCAR) Whole Atmosphere Community Climate Model Extended version (WACCM-X) and the thermosphere-ionosphere-mesosphere electrodynamics general circulation model (TIME-GCM) is used to simulated the 2009 SSW in order to address several outstanding questions pertaining to atmosphere-ionosphere coupling during SSWs. The 2009 SSW was an extreme event, and its influence on the middle and upper atmosphere has been extensively studied in both models and observations [*Chau et al.*, 2010; *Goncharenko et al.*, 2010b; *Manney et al.*, 2009; *Sassi et al.*, 2013; *Jin et al.*, 2012; *Fuller-Rowell et al.*, 2011]. It thus represents an ideal test case. We first investigate the role of the M_2 lunar tide on ionosphere variability during the 2009 SSW. Although *Pedatella and Liu* [2013] found that, on average, the M_2 lunar tide contributes up to ~30% of the ionosphere response to SSWs, *Forbes and Zhang* [2012] found that during the 2009 SSW the M_2 lunar tide obtained amplitudes of up to 40–60 m s^{-1} in zonal wind at *E* region altitudes. Such a dramatic enhancement suggests that the M_2 lunar tide may have a considerable impact on the ionosphere variability during the 2009 SSW. We additionally investigate the role of changes in *F* region meridional neutral winds and thermospheric

composition on the changes in ionospheric electron density during the 2009 SSW. Our simulations illustrate that factors other than tidally induced changes in ionospheric electric fields contribute to *F* region electron density variability during the 2009 SSWs, and thus provide insight into additional processes that are potentially important for atmosphere-ionosphere coupling during SSWs.

2. Model Simulations

The NCAR TIME-GCM is a three-dimensional time-dependent global model of the mesosphere, thermosphere, and ionosphere including self-consistent electrodynamics. The TIME-GCM uses pressure coordinates in the vertical direction, and the vertical domain extends from 10 hPa to $\sim 4 \times 10^{-10}$ hPa. This corresponds to altitudes of roughly 30 km to 400–700 km, with the altitude of the model upper boundary varying based on solar conditions. A detailed overview of the TIME-GCM is provided by *Roble* [1995] and *Roble and Ridley* [1994] and is not repeated herein. The TIME-GCM simulations performed in the present study use a horizontal resolution of 2.5° in latitude and longitude and a vertical resolution of 0.25 scale height. The simulations are performed for fixed solar minimum ($F_{10.7} = 75 \times 10^{-22}$ Wm^{-2} Hz^{-1}) and geomagnetically quiet conditions. January and February 2009 were characterized by low, and quiet, solar and geomagnetic conditions. The neglect of any solar or geomagnetic variations is therefore a reasonable assumption and allows us to clearly distinguish the ionosphere variability that occurs in response to the 2009 SSW.

To simulate the 2009 SSW in the TIME-GCM, hourly output (geopotential height, temperature, and zonal and meridional winds) from WACCM-X simulations of the 2009 SSW are applied at the model lower boundary (10 hPa). The WACCM-X simulations were constrained by nudging WACCM-X toward a combined reanalysis of the Navy Operational Global Atmospheric Prediction System-Advanced Level Physics High Altitude (NOGAPS-ALPHA) and the NASA Modern Era Retrospective Analysis for Research and Applications (MERRA), and thus reproduce the dynamical variability of the 2009 SSW. The reader is referred to *Sassi et al.* [2013] for details regarding the WACCM-X simulations. In addition to forcing the model lower boundary, the TIME-GCM zonal mean zonal and meridional winds and temperatures are nudged toward the WACCM-X zonal means up to an altitude of ~95 km. The nudging is done using the same approach as *Pedatella and Liu* [2013] and is necessary to ensure that the TIME-GCM reproduces the dynamical variability during the 2009 SSW. Note that we only nudge the zonal means, as opposed to the full fields, to permit experiments with an additional lunar semidiurnal tide forcing as described below.

Observations and simulations reveal that the M_2 was dramatically enhanced during the 2009 SSW [*Forbes and Zhang*, 2012; *Sathishkumar and Sridharan*, 2013]. The M_2 enhancement is thus important to consider in simulating the ionosphere perturbations during the 2009 SSW. To illustrate the role of the M_2 on the ionosphere during the 2009 SSW, we have performed two simulations: one with and one without an additional M_2 forcing at the TIME-GCM lower boundary. Note that the WACCM-X simulation used to constrain the TIME-GCM does not include any gravitational lunar tides, and it is thus necessary to add an additional forcing to the TIME-GCM. In the simulation without any lunar tide forcing, the TIME-GCM lower boundary is only forced by WACCM-X as previously described. The additional M_2 forcing for the simulation with the lunar tide comes from the global scale wave model (GSWM) simulations of *Forbes and Zhang* [2012]. The two simulations are identical except for the M_2 forcing, and by comparing the two simulations, we are able to clearly demonstrate the impact of the M_2 on ionosphere variability during the 2009 SSW. A third simulation was also performed using climatological zonal means, as well as migrating diurnal and semidiurnal solar tides from GSWM-02 [*Hagan and Forbes*, 2002, 2003]. This simulation serves as a control simulation and does not include the effects of the SSW. We present differences relative to the control simulation to clearly illustrate the effects of the SSW on the ionosphere and eliminate any longer-term seasonal variability from the simulations.

3. Observations

The TIME-GCM simulations are compared with observations from the Jicamarca Radio Observatory (11.95°S and 76.87°W geographic; 1.92°S magnetic latitude) incoherent scatter radar (ISR) and global satellite observations from the Constellation Observing System for Meteorology, Ionosphere, and Climate (COSMIC). The Jicamarca ISR measures vertical plasma drifts every 5 min using the technique described by *Kudeki et al.* [1999]. The daytime vertical plasma drifts are averaged over the altitude range of 200 to 400 km. The Jicamarca vertical plasma drifts during the 2009 SSW have previously been presented by *Chau et al.* [2010].

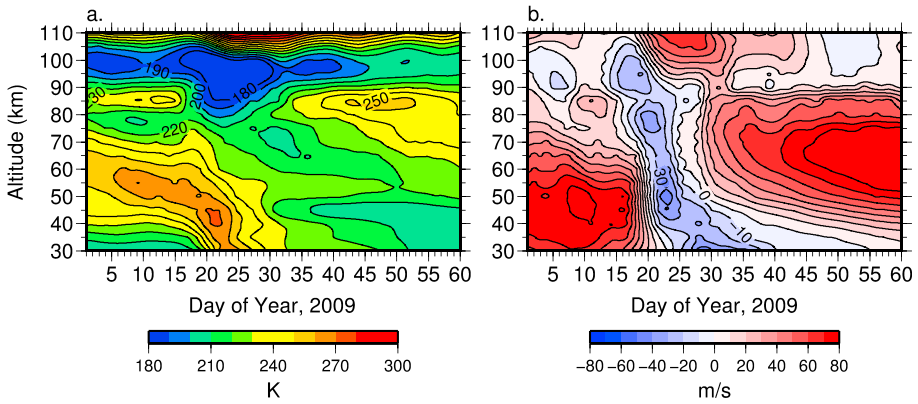

Figure 1. (a) TIME-GCM zonal mean temperature averaged between 70 and 80°N latitude. (b) TIME-GCM zonal mean zonal wind at 60°N latitude.

Vertical plasma drift anomalies from the empirical model of *Scherliess and Fejer* [1999] are presented in section 4.2.

To complement the Jicamarca ISR observations, we use global ionosphere observations from the COSMIC satellites. COSMIC is a six-satellite constellation that observes the neutral atmosphere and ionosphere using the technique of Global Positioning System (GPS) radio occultation [*Rocken et al.*, 2000; *Anthes et al.*, 2008]. The Abel inversion is used to obtain electron density profiles from the GPS observations [*Schreiner et al.*, 1999]. For the present study, we use the retrieved maximum *F* region electron density (NmF2), which is not significantly impacted by the assumption of spherical symmetry in the Abel inversion [*Yue et al.*, 2010]. COSMIC observations have previously been used to study the 2009 SSW by, for example, *Yue et al.* [2010], *Jin et al.* [2012], and *Lin et al.* [2012]. The COSMIC observations are binned using a 5 day running mean in 2.5° magnetic latitude and 1 h local time (LT) bins. Longitude variability is neglected in order to reduce the temporal window of the running average.

4. Results and Discussion

4.1. Zonal Mean and Tidal Variability

Vertical profiles of the zonal mean temperature averaged between 70° and 80°N latitude and zonal mean zonal wind at 60°N latitude are shown in Figure 1. The results in Figure 1 are from the TIME-GCM simulation nudged by WACCM-X. The descent of the stratopause beginning around day 15, along with the formation of an elevated stratopause around day 35 can clearly be seen in Figure 1a. A mesospheric cooling occurs between days 20 and 30, and this coincides with the SSW. The deceleration of the eastward stratospheric winds and reversal to westward winds around day 20–25 can be seen in Figure 1b. The reversal of the eastward stratospheric winds to westward is accompanied by a reversal of the mesospheric winds from westward to eastward. The results shown in Figure 1 are generally consistent with observations as well as different whole atmosphere model simulations of the 2009 SSW [*Smith et al.*, 2009; *Pedatella et al.*, 2014] and demonstrate that the approach employed in the present study is able to reproduce the zonal mean dynamical variability during the 2009 SSW in the TIME-GCM.

The *SW*2 and M_2 amplitudes and phases in zonal wind at 110 km are shown in Figure 2 for January and February 2009. Note that the results in Figure 2 are based on determining the full spectrum of tides using a running 14.75 day window. The fit window is roughly half of a lunar cycle and is necessary in order to separate the *SW*2 and M_2 tides. For the *SW*2 (Figures 2a and 2b), the TIME-GCM simulations reveal enhancements at middle-high latitudes in both hemispheres during the SSW. The maximum amplitudes occur around days 25–27 in the Southern Hemisphere, and 1 to 2 days later in the Northern Hemisphere. The *SW*2 attains amplitudes of ~50 m s^{-1} in the Northern Hemisphere, and ~45 m s^{-1} in the Southern Hemisphere. These enhancements represent an approximate doubling of the *SW*2 amplitude compared to conditions prior to the SSW in early January. We note that the maximum *SW*2 amplitudes occur after the onset of major SSW conditions (day 24), and this is consistent with other numerical simulations of the 2009 SSW [*Pedatella et al.*, 2014]. However, unlike other simulations, the TIME-GCM simulations only indicate a weak decrease in the

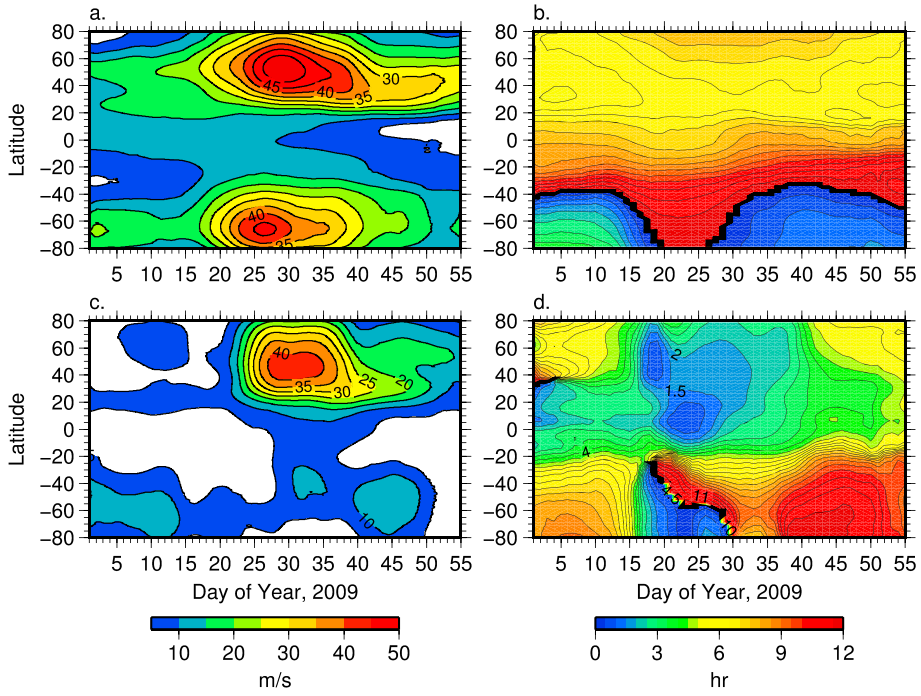

Figure 2. (a) Amplitude and (b) phase of the migrating semidiurnal solar tide (*SW*2) in zonal wind at 110 km. (c and d) Same as Figures 2a and 2b except for the migrating semidiurnal lunar tide (M_2).

Southern Hemisphere *SW*2 prior to the SSW. This may be related to the fact that this decrease is not strong in the WACCM-X simulations used as forcing for the TIME-GCM. Variability in the *SW*2 phase is especially apparent in the Southern Hemisphere where the phase decreases by several hours around the time of the SSW. In the Northern Hemisphere, the phase is nearly constant, although it does increase by ~1 h around the time of the SSW.

Large changes also occur in the TIME-GCM simulated M_2 during the SSW (Figures 2c and 2d). At middle-high latitudes in the Northern Hemisphere, the M_2 amplitude reaches ~40 m s^{-1} around day 30. This represents a several times increase of the M_2 amplitude due to the SSW. The M_2 enhancement during the 2009 SSW is thus significantly greater than the simulated enhancement for an average SSW [e.g., *Pedatella et al.*, 2012; *Pedatella and Liu*, 2013]. The drastic enhancement in the M_2 during the 2009 SSW in our simulations is, however, consistent with the prior simulations of *Forbes and Zhang* [2012]. The M_2 phase is shifted earlier by several hours during the SSW. The changes in the M_2 amplitude and phase can be attributed to the influence of changes in the background zonal mean atmosphere during the SSW [*Forbes and Zhang*, 2012]. Given that the M_2 obtains amplitudes that are nearly equivalent to the *SW*2, we can conclude that the M_2 is an important contributor to the MLT dynamics during the 2009 SSW and is also likely to influence variability in the ionosphere.

4.2. Ionosphere Variability

We now turn our attention to the ionosphere variability simulated by the TIME-GCM. The simulated and observed changes in vertical plasma drift velocity at Jicamarca are shown in Figure 3. Results for the TIME-GCM simulations with and without the GSWM lunar tide forcing are shown in Figures 3a and 3b, respectively. Note that the TIME-GCM results shown in Figure 3, and subsequent figures, are differences with respect to the TIME-GCM simulation forced only with GSWM-02 migrating diurnal and semidiurnal tides. A 3 day smoothing has also been applied in Figures 3a and 3b to make the salient features more apparent. The observations (Figure 3c) indicate an initial decrease in the vertical plasma drift velocity in the morning and an increase in the afternoon. The morning decrease progresses toward later local times beginning around day 20. The initial suppression of the morning vertical plasma drift velocities is replaced by an increase in the morning vertical plasma drift velocities beginning around day 25. The local time of the maximum enhancement progresses toward later local times over several days.

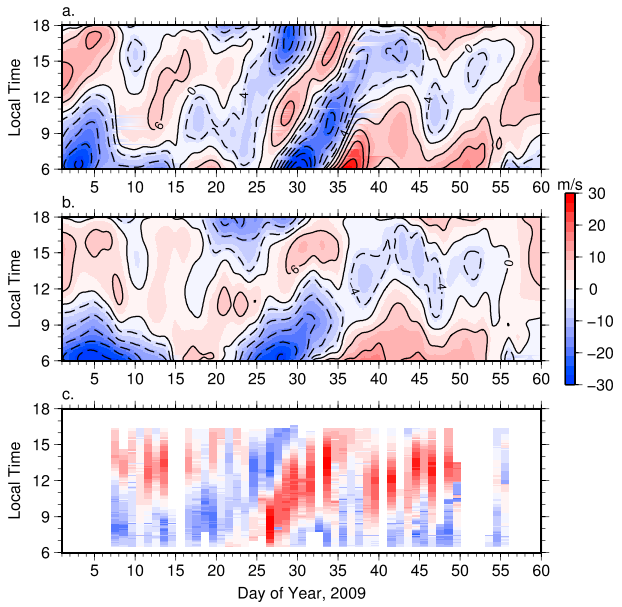

Figure 3. (a) TIME-GCM-simulated changes in the 300 km equatorial vertical plasma drift velocity at 75°W longitude for the simulation with lunar tides. (b) Same as Figure 3a except for the simulation without lunar tides. (c) Observed change in the vertical plasma drift velocity at Jicamarca Radio Observatory.

The two TIME-GCM simulations show an enhancement in the morning vertical plasma drift velocity that progresses toward later local times, as well as a decrease in the afternoon vertical plasma drift velocity. In this sense, both of the TIME-GCM simulations are characteristically similar to the Jicamarca ISR observations. There are, however, notable differences in the timing of the vertical plasma drift velocity perturbations in the two TIME-GCM simulations. In particular, the simulation without the lunar tide (Figure 3b) shows an increase in the morning vertical plasma drift velocity from days 15–20 that slowly progresses toward later local times beginning around day 20. The progression of the vertical drift enhancement toward later local times is attributed to changes in the *SW*2 amplitude and phase [*Pedatella and Liu*, 2013]. The morning vertical drift enhancements are replaced by a decrease in the morning vertical plasma drift velocity that occurs between days 22–32. The timing of the increase and decrease of the vertical plasma drift velocities for the simulation without lunar tide forcing is thus in disagreement with the observations. The timing of the vertical plasma drift velocity perturbations is significantly improved for the simulation with lunar tide forcing (Figure 3a). In this simulation, the enhancement of morning vertical plasma drift velocity perturbations, and a progression toward later local times, does not occur until around day 25. The decrease in the morning vertical plasma drift velocity is also delayed until day 28, which is in better agreement with the observations. The rate that the vertical plasma drift anomalies progress toward later local times is also more consistent with the observations in the simulation that includes lunar tide forcing. This comparison leads us to conclude that, for the 2009 SSW, the lunar tide is an important contributor to variability in the low-latitude ionosphere. Although the TIME-GCM simulations capture many of the general features of the observed vertical plasma drift velocity perturbations during the 2009 SSW, there remain some notable differences between the simulations and observations. The most notable differences are the absence of the initial decrease in early morning vertical plasma drifts between days 15 and 20, and an apparent shift in the onset of the progression of the vertical drift anomalies toward later local times, which occur a few days later in the simulations compared to the observations. Despite these differences, the overall agreement between the TIME-GCM simulation with lunar tide forcing and the Jicamarca ISR observations demonstrates that the simulations are generally able to reproduce the ionosphere variability during the SSW.

The zonal mean NmF2 observed by the COSMIC satellites and simulated by the TIME-GCM at 10 and 18 LT is shown in Figure 4. The results at 10 and 18 LT are considered as representative of the morning and afternoon/evening electron density variability. The results at other local times are similar and lead to similar conclusions. All of the results shown in Figure 4 are based on a 5 day running mean, and no background has been removed. Although the temporal resolution is relatively coarse, Figure 4 provides a global comparison to complement the results from a single location that were presented in Figure 3. Results for the TIME-GCM simulations with (Figures 4a and 4d) and without (Figures 4b and 4e) the M_2 lunar tide forcing are again presented for comparison with the observations. It is first apparent that the TIME-GCM generally underestimates the NmF2 compared to the observations; however, we are interested in the temporal variability due to the SSW, and the slight underestimation of the NmF2 in the simulations is not of concern. At 10 LT, the COSMIC observations reveal enhanced NmF2 in the northern and southern equatorial ionization anomaly (EIA) crests around days 25–30 and another enhancement near day 40. A decrease in the EIA trough

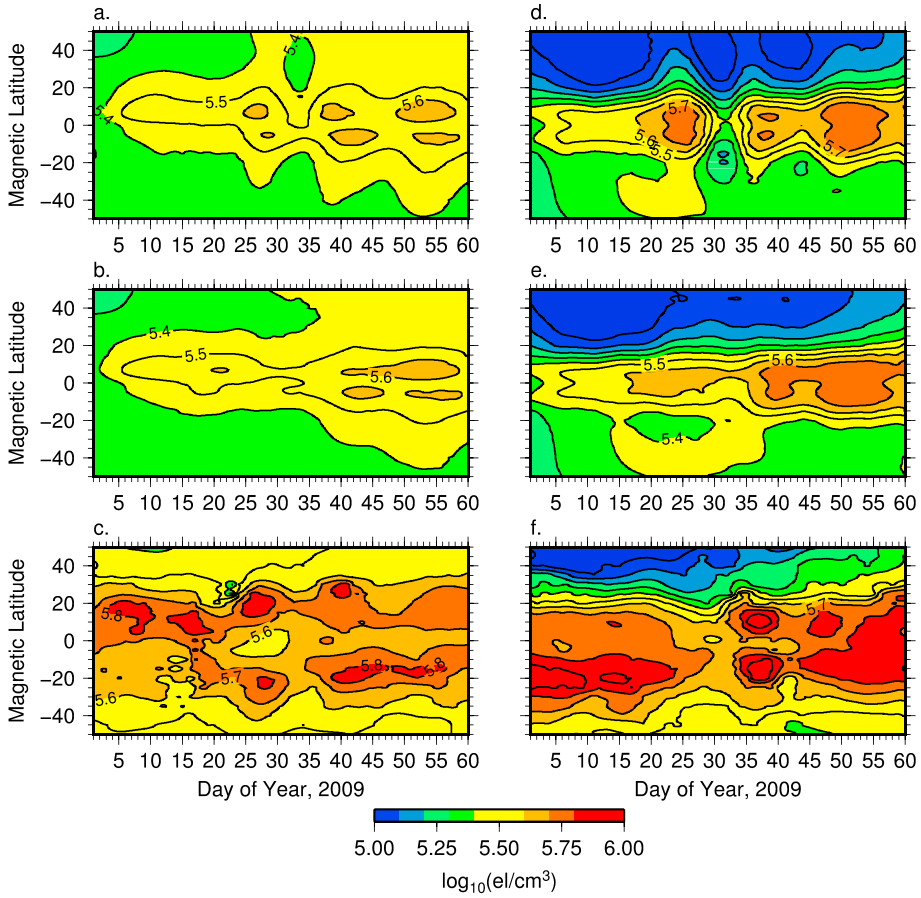

Figure 4. (a) TIME-GCM-simulated zonal mean NmF2 at 10 LT for the simulation with lunar tides. (b) Same as Figure 4a except for the simulation without lunar tides. (c) Zonal mean NmF2 at 10 LT from COSMIC observations. (d–f) Same as Figures 4a–4c) except for at 18 LT. Results are 5 day moving average.

also occurs between days 25 and 30. The enhancement at 10 LT around the time of the SSW (days 25–30) is consistent with previous observations [*Goncharenko et al.*, 2010a; *Lin et al.*, 2012]. At 18 LT (Figures 4d–4f), the COSMIC observations reveal a decrease in the low-latitude zonal mean NmF2 between days 25 and 35, followed by a strong increase from days 35 to 40. We again note that the decrease in afternoon electron density around the time of the SSW peak is consistent with prior observations [*Goncharenko et al.*, 2010a; *Lin et al.*, 2012]. Only a small decrease in NmF2 at 18 LT occurs around the time of the SSW in the simulation without the M_2. A strong decrease occurs in the TIME-GCM simulation with lunar tides, and the timing of the maximum decrease is around day 30, which is consistent with the COSMIC observations. However, this simulation shows an increase around day 25 that is not apparent in the observations. Both TIME-GCM simulations capture the enhancement on days 35–40 and after day 45. These enhancements are stronger, and more consistent with the observations, in the simulation with lunar tide forcing. Considering the results in Figures 3 and 4, we can conclude that the M_2 lunar tide significantly influences the ionosphere response to the 2009 SSW. Furthermore, the results demonstrate that including the M_2 is important for modeling the ionosphere response to the 2009 SSW, at least in our WACCM-X/TIME-GCM simulations.

4.3. Sources of Electron Density Variability

The *F* region electron density variability that occurs during SSWs is typically attributed to changes in atmospheric tides which influence the dynamo generation of electric fields. The resulting influence on equatorial vertical plasma drifts is thought to generate the changes in equatorial and low-latitude electron densities [*Chau et al.*, 2012]. This mechanism is supported by the large changes in semidiurnal tides (Figure 2) and the predominately semidiurnal nature of the equatorial vertical plasma drift (Figure 3) and electron density (Figure 4) variability during SSWs. While this mechanism may be the dominant driver of the electron density variability, it is important to consider the potential role of additional mechanisms. In particular, in this

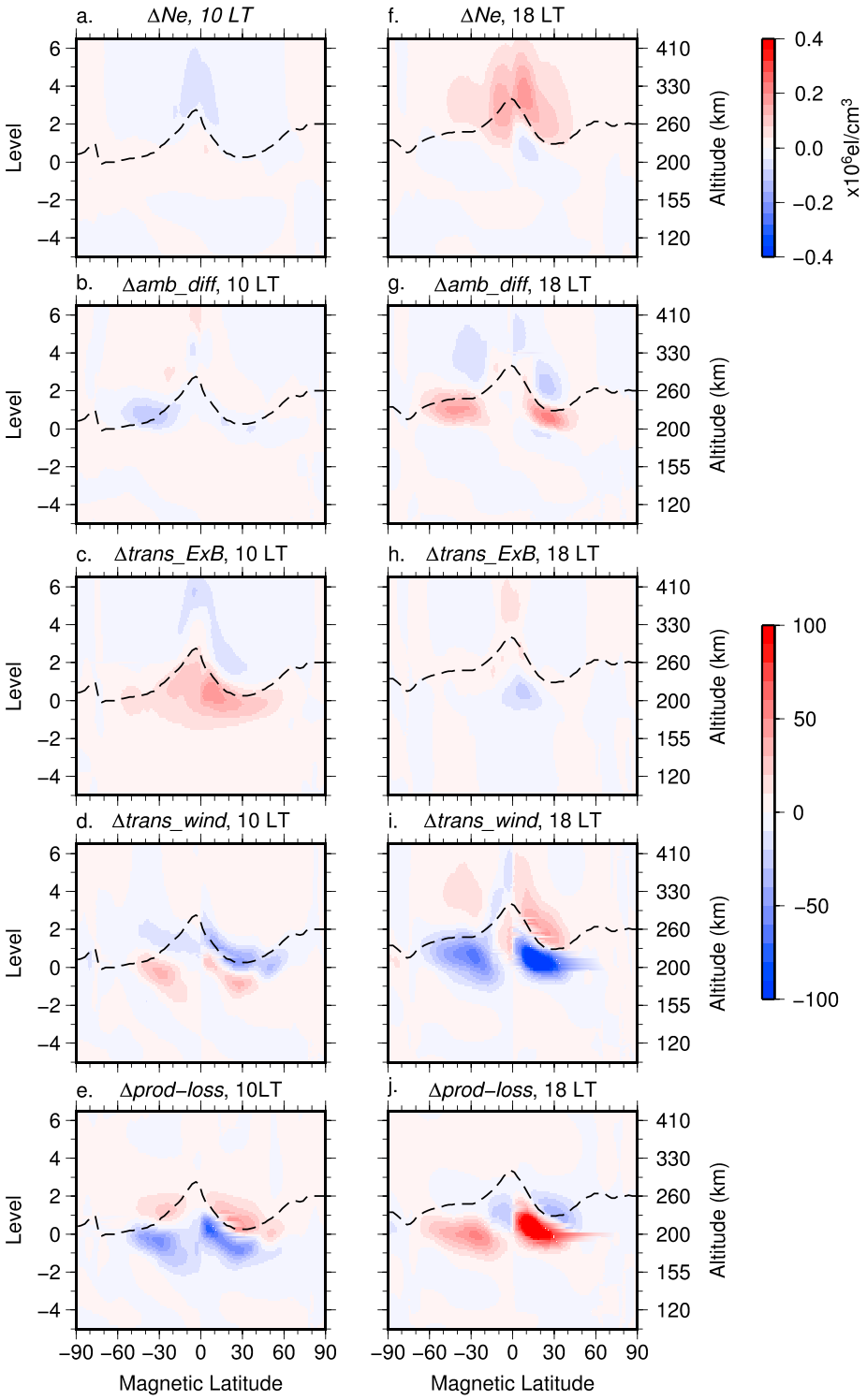

Figure 5. TIME-GCM-simulated changes in the zonal mean (a) electron density, (b) amb_diff (c) trans_E × B, (d) trans_wind, and (e) prod-loss at 10 LT on day 24. (f–j) Same as Figures 5a–5e except for at 18 LT. Results are for the TIME-GCM simulation with lunar tide forcing.

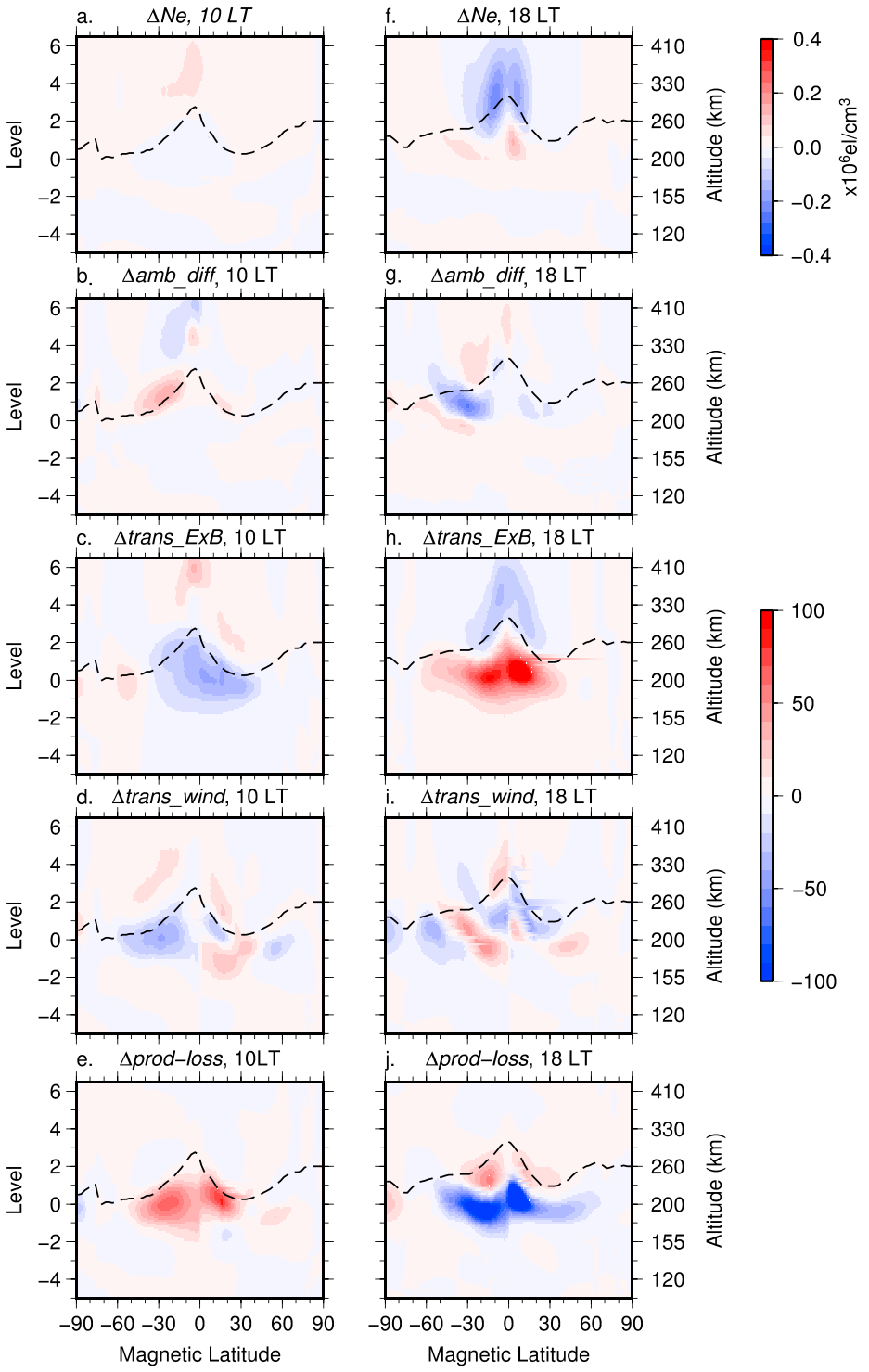

Figure 6. Same as Figure 5 except on day 29.

section we seek to understand what, if any, influence meridional winds and thermosphere composition may have on the ionosphere electron density variability during the 2009 SSW. To investigate the role of alternative sources of the electron density variability, we perform a term analysis of the ion continuity equation. Following *Lei et al.* [2008], the *F* region ion density changes are described by the ion continuity equation:

$$\frac{\partial N}{\partial t} = q - \beta N - \nabla \cdot (N\vec{V}) \quad (1)$$

where N is the ion concentration, β is the loss coefficient, and q is the rate of production. The βN term represents the loss rate. The final term in equation (1) represents effects due to transport by electric fields, neutral winds, and ambipolar diffusion. We are only interested in the electron density changes occurring in the F region where the ion composition is dominated by O^+ ions. We thus only perform a term analysis of the ion continuity equation for O^+. Considering only O^+, equation (1) can be written as

$$\frac{\partial N_{O^+}}{\partial t} = q_{O^+} - \beta_{O^+} N_{O^+} - \nabla \cdot (N_{O^+} \vec{V}_{O^+}) \tag{2}$$

Similar to *Lei et al.* [2008], we will refer to the terms q_{O^+} and $\beta_{O^+} N_{O^+}$ as production and loss, respectively. The transport term ($\nabla \cdot (N_{O^+} \vec{V}_{O^+})$) is further broken down into transport by electric fields (trans_E × B), neutral winds (trans_wind), and ambipolar diffusion (amb_diff). The rate of change of O^+ can thus be written as

$$\frac{\partial N_{O^+}}{\partial t} = \text{production} - \text{loss} + \text{trans\_E} \times \text{B} + \text{trans\_wind} + \text{amb\_diff} \tag{3}$$

Figures 5–7 show zonal mean changes in electron density, amb_diff, trans_E × B, trans_wind, and production-loss on days 24, 29, and 32, respectively. The changes are relative to the TIME-GCM control simulation. Results are shown at 10 LT (Figures 5a–5e, 6a–6e, and 7a–7e), and 18 LT (Figures 5f–5j, 6a–6e, and 7f–7j). Note that in Figures 5–7, the results are presented in terms of the model pressure levels as this is a more appropriate coordinate for the analysis, especially when analyzing the neutral composition. Approximate altitudes and the F region peak height (dashed black lines) are also included as a reference. On day 24, the electron density changes are as expected, with a slight decrease at 10 LT and a considerably larger increase at 18 LT. The electron density changes are largest near, and slightly above, the F region peak height at low latitudes. Considering the terms of the continuity equation, the changes in amb_diff are small and tend to oppose the electron density changes. At 10 LT, trans_E × B decreases above, and increases below, the F region peak. This is consistent with the decrease in vertical plasma drift velocity that occurred on this day and local time (see Figure 8 for zonal mean vertical plasma drift perturbations which are slightly different then those at the location of Jicamarca). Only small changes occur in the trans_E × B term at 18 LT, and this is expected given the minimal change in vertical plasma drift velocity. Large changes are also apparent in both the trans_wind and production-loss terms at both local times, and these are especially large at 18 LT. The source of these changes will be discussed in more detail later. From comparing the change in electron density with the changes in the different terms of the ion continuity equation in Figure 5, it can be seen that the electron density changes represent the combined effects of several different mechanisms. At low latitudes, near, and above, the F region peak, the change in electron density is primarily driven by changes in transport due to electric fields (trans_E × B) and meridional neutral winds (trans_wind). Below the F region peak, changes in transport due to electric fields and meridional neutral winds are again the largest contributor to the changes in electron density. However, at these altitudes changes in production-loss tend to oppose the trans_E × B and trans_wind changes, resulting in generally small electron density changes below the F region peak.

On day 29, there is almost no change in the electron density at 10 LT (Figure 6a), while the electron density at 18 LT is decreased significantly above the F region peak (Figure 6f). The electron density changes again primarily occur at low latitudes near the F region peak. At 10 LT, the vertical plasma drift increase (Figure 8) leads to a decrease in the electron density below the F region peak, and this is reflected in the trans_E × B changes shown in Figure 6c. This decrease is compensated by an increase in the production-loss term, leading to no net electron density changes. We will discuss the mechanism behind the production-loss changes later. The decrease in vertical plasma drift velocity at 18 LT on day 29 (Figure 8) results in the trans_E × B term increasing below the F region peak and decreasing in the topside ionosphere. The vertical plasma drift changes are large (~12–15 m s^{-1}), and changes in the trans_E × B term thus account for the majority of the changes in electron density near and above the F region peak. Notable changes are also apparent in the trans_wind and production-loss terms at 18 LT, and these changes will be discussed in more detail later. We note that below the F region peak, changes in the production-loss term again tend to generally oppose the changes in the trans_E × B term, leading to small electron density changes below the F region peak. The results for day 32 (Figure 7) are generally similar to those on days 24 and 29. That is, the electron density changes are again dominated by changes in the trans_E × B term. Changes in the trans_wind

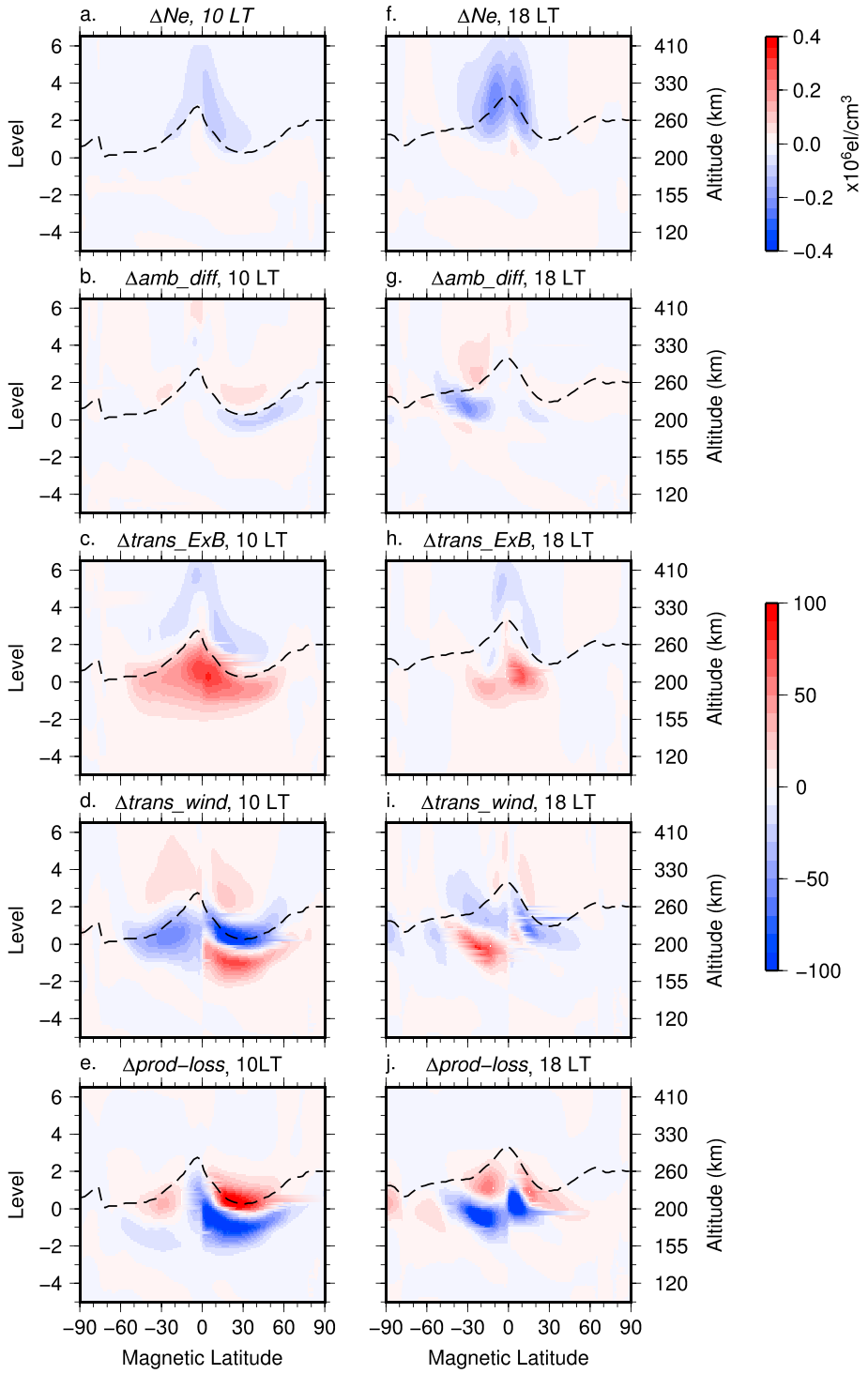

Figure 7. Same as Figure 5 except on day 32.

and production-loss terms are again not negligible, suggesting that neutral wind and composition changes contribute to the *F* region electron density variability during the 2009 SSW.

We now turn our attention toward understanding the changes in the trans_wind and production-loss terms in Figures 5–7. Zonal mean meridional winds on TIME-GCM pressure level 4.0 (~325 km) at 10 and 18 LT are shown in Figure 9. Raw winds are shown in Figures 9a and 9b, and the perturbations relative to the control run are shown in Figures 9c and 9d. The results in Figure 9 reveal meridional wind changes in excess of

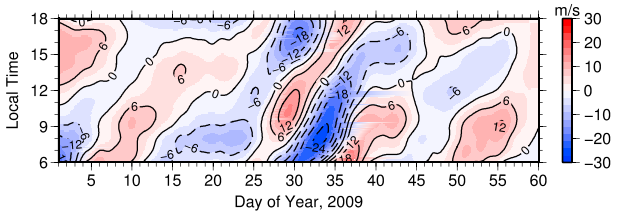

Figure 8. TIME-GCM-simulated change in the zonal mean vertical plasma drift velocity at the magnetic equator and 300 km. Results are for the TIME-GCM simulation with lunar tide forcing.

50 m s^{-1} occur around the SSW. Note that the meridional wind changes are expected based on the changes in the trans_wind term that are shown in Figures 5–7, and the results in Figure 9 serve to illustrate the latitudinal and local time variability of the meridional winds that produce the trans_wind changes. The latitudinal variation of the meridional wind anomalies on days 24 (black), 29 (red), and 32 (blue) are shown in Figures 9e and 9f, and these can be used to provide a clear understanding of the wind changes that generate the changes in the trans_wind term in Figures 5–7. In the Northern Hemisphere an increase (i.e., larger northward winds) in the meridional winds will decrease the electron density in the topside ionosphere and increase the electron density in the bottomside ionosphere. The opposite occurs in the Southern Hemisphere. First, considering the results at 10 LT, it can be seen in Figure 9e that the meridional wind becomes more southward in the Southern Hemisphere and more northward in the Northern Hemisphere on day 24. The opposite response occurs on days 29 and 32. This leads to the decrease (increase) in the trans_wind term in the topside (bottomside) ionosphere on day 24, and the increase (decrease) in the topside (bottomside) ionosphere on days 29 and 32. At 18 LT, the direction of the meridional wind anomalies is reversed, and this suggests that the meridional wind anomalies are driven by a change in the semidiurnal tides at *F* region altitudes. Results (not shown) reveal that the semidiurnal tide amplitude increases around day 30, and this increase is largest in the Southern Hemisphere and equatorial region where the meridional wind anomalies are largest. The reversal of the meridional wind anomalies at 18 LT means that the winds act to increase the topside ionosphere electron density on day 24 and decrease the topside ionosphere electron density on days 29 and 32. The wind anomalies are generally consistent with the changes in the trans_wind term, and we therefore conclude that changes in meridional winds at *F* region altitudes contribute to the electron density variability during SSWs.

We conclude our analysis of the ionosphere term analysis with a discussion of the changes in the production-loss term. To explain these changes, the relative change in production, loss coefficient (β), and O/N_2 at 18 LT on days 24 and 32 are shown in Figure 10. Note that we show changes in β rather than changes

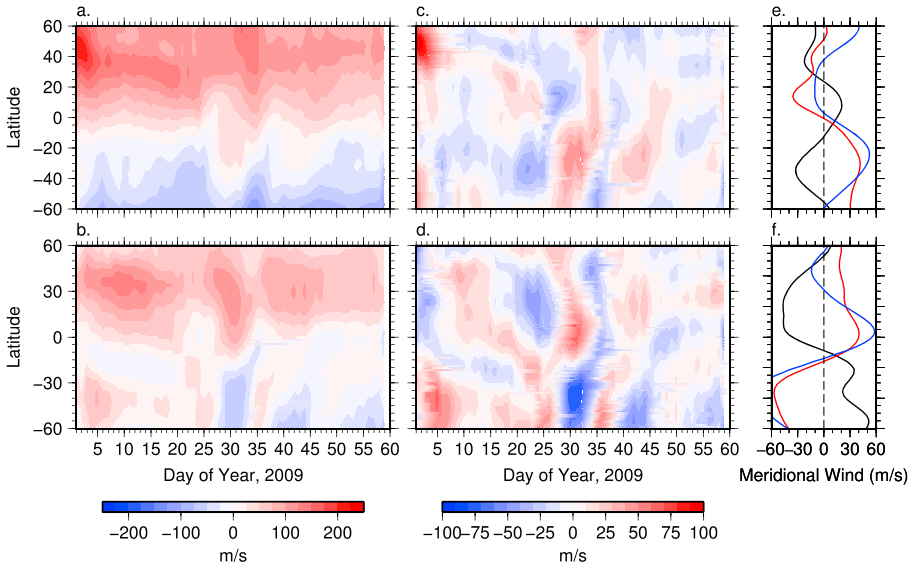

Figure 9. TIME-GCM simulated zonal mean meridional neutral wind at pressure level 4.0 (~325 km) at (a) 10 LT and (b) 18 LT. The meridional wind difference relative to the TIME-GCM control simulation at (c) 10 LT and (d)18 LT. Latitudinal profile on day 24 (black), 29 (red), and 32 (blue) at (e) 10 LT and (f) 18 LT. Results are for the TIME-GCM simulation with lunar tide forcing.

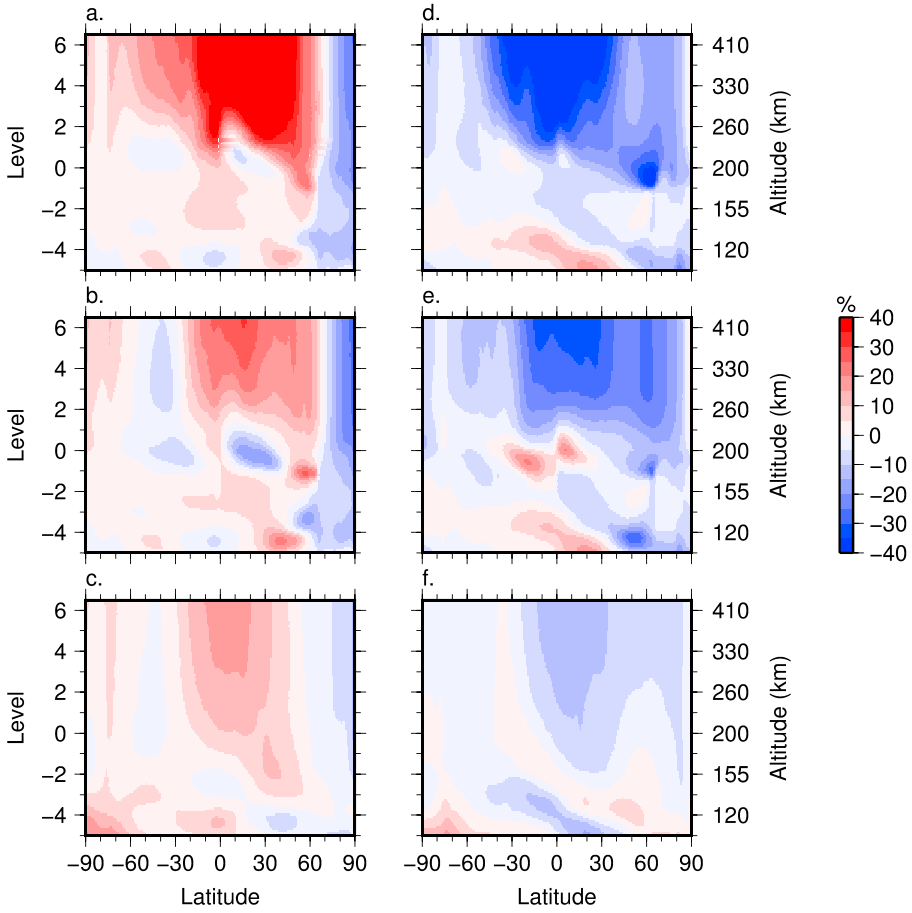

Figure 10. TIME-GCM-simulated change in zonal mean (a) production, (b) loss coefficient (β), and (c) O/N_2 at 18 LT on day 24. (c–f) Same as Figures 10a–10c except for on day 32. Results are for the TIME-GCM simulation with lunar tide forcing.

in loss since β is directly influenced by the thermosphere composition, while changes in the loss ($= \beta N_{O^+}$) term incorporate changes in the ion composition. Days 24 and 32 are chosen to represent different features of the role of composition changes on the electron density variability during the SSW. On day 24, the production term increases at low to middle latitudes, while it decreases at high latitudes in the Northern Hemisphere. A slight decrease also occurs at low to middle latitudes slightly below the *F* region peak (levels 0–1). The changes in β are generally similar to those of the production term, indicating that as the rate of production is increased, the loss rate is also enhanced. Similar to the changes in production and β, O/N_2 increases at low to middle latitudes and decreases at high latitudes in the Northern Hemisphere. The connection between the O/N_2 changes and those in production and β will be discussed below. At low to middle latitudes, the opposite response occurs on day 32 compared to day 24. However, a decrease in production, β, and O/N_2 still occurs at high latitudes in the Northern Hemisphere. The influence of the O/N_2 changes on production and β can be explained as follows. An increase in O will increase the rate of O^+ production, and an increase in N_2 will increase the loss of O^+. Increases in O are thus related to an increase in the production term, and increases in N_2 will increase β. If the increase in O/N_2 on day 24 is related to an increase in O and decrease in N_2, then both the rate of production and loss will be increased, and this is what occurs as seen in Figures 10a and 10b. Likewise, on day 32, if the low-middle latitude O/N_2 decrease is driven by a decrease in O and increase in N_2, then both the rate of production and loss will decrease. Analysis of the simulation results reveals that O increases on day 24, and decreases on day 32, and that the opposite changes occur in N_2. We therefore consider the simultaneous increase and decrease of O and N_2 to be responsible for generating the changes in production, β, and O/N_2. This mechanism is supported by the simulated tidal variability and prior studies. *Forbes et al.* [1993] and *Yamazaki and Richmond* [2013] found that the dissipation of upward propagating tides leads to a decrease in O and increase in N_2, resulting in a decrease in O/N_2.

This decrease is due to the dissipation of tides which modify the global circulation and induce a downward transport of O [*Yamazaki and Richmond*, 2013]. Considering these prior studies, we consider the large O/N_2 decrease on day 32 to be driven by the enhanced tidal amplitudes that occur on this day (Figure 2). The large tidal amplitudes lead to enhanced tidal mixing, resulting in the O/N_2 decrease. The decrease in O/N_2 causes the decrease in production and β. The slight increase in O/N_2 at midlatitudes that occurs on day 24 may be related to slightly weaker tidal mixing. We again note that the O/N_2 increase leads to the increase in production and β. Last, we note that on both days the O/N_2 is significantly reduced at high latitudes in the Northern Hemisphere. These changes may not be related to the same tidal dissipation mechanism that drives the O/N_2 changes at middle-low latitudes. They may be more directly related to the SSW in terms of temperature changes, planetary wave, and/or gravity wave effects, and additional research is required to further understand the high-latitude O/N_2 changes during SSWs.

5. Summary and Conclusions

Simulations and observations of the ionosphere response to the 2009 SSW are presented in the current study. The simulations combine WACCM-X, which is constrained by NOGAPS-ALPHA/MERRA reanalysis, with the TIME-GCM. The simulations are compared with Jicamarca ISR vertical plasma drift velocities and global NmF2 observations from the COSMIC satellites. The simulation results generally reproduce the observed ionosphere variability, and the agreement between the observations and simulations is considerably improved when the M_2 lunar tide is included in the simulations. The M_2 reaches amplitudes of $\sim$40 m s^{-1} in zonal wind at *E* region altitudes, and it is thus not surprising that the M_2 significantly influences the ionosphere variability during the 2009 SSW. Although ionosphere variability occurs in the absence of the M_2, inclusion of the M_2 changes the nature of the ionosphere response to the SSW. This leads us to the conclusion that, at least for the 2009 SSW, the M_2 was an important contributor to the ionosphere variability. However, it should be noted that the 2009 SSW was a rather extreme event, and for more moderate SSWs we would not anticipate such a large M_2 enhancement. A smaller M_2 enhancement will likely reduce its importance for producing ionosphere variability during more moderate SSWs. During moderate SSWs, the ionosphere variability is due to the combined effects of the *SW*2 and M_2 [e.g., *Pedatella and Liu*, 2013].

Factors driving the changes in *F* region electron density during the 2009 SSW are also investigated in the present study. Based on a term analysis of the ion continuity equation, we examined the impact of changes in ambipolar diffusion, electric fields, neutral winds, production, and loss on *F* region electron density variability during the SSW. Consistent with the current prevailing theory, the electron density changes at low latitudes were found to be primarily driven by electric field changes. The electric field changes are related to variability in the *SW*2 and M_2 tides which influence the dynamo generation of electric fields in the *E* region. Though electric field changes are the dominant source of the electron density variability, the simulations reveal that changes in *F* region meridional winds and thermosphere composition (O/N_2) also contribute to changes in electron density during the SSW. Our results therefore indicate additional mechanisms for generating *F* region electron density variability during SSWs that have not previously been considered. Additional observation and modeling research on *F* region meridional wind and O/N_2 changes during SSWs is therefore necessary in order to further understanding of these changes and their influence on the electron density variability.

Acknowledgments

Simulation output in NetCDF is archived on the National Center for Atmospheric Research High Performance Storage System and is available on request. The COSMIC observations used in the present study are available through the COSMIC Data Analysis and Archival Center (http://cdaac-www.cosmic.ucar.edu/cdaac/). Observations from the Jicamarca ISR are from the Madrigal Database (http://jro.igp.gob.pe/madrigal/). N.P. acknowledges support from the National Science Foundation grant AGS-1033112. Additional support from NSF grant AGS-1138784 and NASA/LWS grant NNX09AJ83G (H.L.) NASA/LWS grant NNH12AT21L (F.S. and H.L.) is acknowledged. F.S. acknowledges also the support of 6.1 funding from the Office of Naval Research. This work was supported in part by a grant of computer time from the DOD High Performance Computing Modernization Program at the US Navy DOD Supercomputing Resource Center (NAVO). X.Z. was supported under grant ATM-0719480 from the National Science Foundation to the University of Colorado. The Jicamarca Radio Observatory is a facility of the Instituto Geofisico del Peru operated with support from the NSF AGS-0905448 through Cornell University. The National Center for Atmospheric Research is sponsored by the National Science Foundation. The International Space Science Institute facilitated discussions related to the present paper by sponsoring a workshop on "Atmosphere-Ionosphere Coupling during Stratospheric Sudden Warmings."

Michael Liemohn thanks Alexey Danilov and another reviewer for their assistance in evaluating this paper.

References

Anthes, R. A., et al. (2008), The COSMIC/FORMOSAT-3 Mission: Early results, *Bull. Am. Meteorol. Soc.*, *89*, 313–333, doi:10.1175/BAMS-89-3-313.

Charlton, A. J., and L. M. Polvani (2007), A new look at stratospheric sudden warmings. Part I: Climatology and modeling benchmarks, *J. Clim.*, *20*, 449–469.

Chau, J. L., B. G. Fejer, and L. P. Goncharenko (2009), Quiet variability of equatorial ExB drifts during a sudden stratospheric warming event, *Geophys. Res. Lett.*, *36*, L05101, doi:10.1029/2008GL036785.

Chau, J. L., N. A. Aponte, E. Cabassa, M. P. Sulzer, L. P. Goncharenko, and S. A. Gonzlez (2010), Quiet time ionospheric variability over Arecibo during sudden stratospheric warming events, *J. Geophys. Res.*, *115*, A00G06, doi:10.1029/2010JA015378.

Chau, J. L., L. P. Goncharenko, B. G. Fejer, and H.-L. Liu (2011), Equatorial and low latitude ionospheric effects during sudden stratospheric warming events, *Space Sci. Rev.*, *168*, 385–417, doi:10.1007/s11214-011-9797-5.

Fejer, B. G., M. E. Olson, J. L. Chau, C. Stolle, H. Lühr, L. P. Goncharenko, K. Yumoto, and T. Nagatsuma (2010), Lunar-dependent equatorial ionospheric electrodynamic effects during sudden stratospheric warmings, *J. Geophys. Res.*, *115*, A00G03, doi:10.1029/2010JA015273.

Fejer, B. G., B. D. Tracy, M. E. Olson, and J. L. Chau (2011), Enhanced lunar semidiurnal equatorial vertical plasma drifts during sudden stratospheric warmings, *Geophys. Res. Lett.*, *38*, L21104, doi:10.1029/2011GL049788.

Forbes, J. M., R. G. Roble, and C. G. Fesen (1993), Acceleration, heating, and compositional mixing of the thermosphere due to upward propagating tides, *J. Geophys. Res.*, *98*(A1), 311–321.

Forbes, J. M., and X. Zhang (2012), Lunar tide amplification during the January 2009 stratosphere warming event: Observations and theory, *J. Geophys. Res.*, *117*, A12312, doi:10.1029/2012JA017963.
Fraser, G. J. (1977), The 5-day wave and ionospheric absorption, *J. Atmos. Terr. Phys.*, *39*, 121–124.
Fraser, G. J., and M. R. Thorpe (1976), Experimental investigations of ionospheric/stratospheric coupling in southern mid latitudes—1. Spectra and cross-spectra of stratospheric temperatures and the ionospheric f-min parameter, *J. Atmos. Terr. Phys.*, *38*, 1003–1011.
Fraser, G. J., and D. S. Wratt (1976), Experimental investigations of ionospheric/stratospheric coupling in southern mid-latitudes—2. Comparison of mesospheric electron densities and drifts with stratospheric temperatures and winds, *J. Atmos. Terr. Phys.*, *38*, 1013–1016.
Fuller-Rowell, T., F. Wu, R. Akmaev, T.-W. Fang, and E. Araujo-Pradere (2010), A whole atmosphere model simulation of the impact of a sudden stratospheric warming on thermosphere dynamics and electrodynamics, *J. Geophys. Res.*, *115*, A00G08, doi:10.1029/2010JA015524.
Fuller-Rowell, T., H. Wang, R. Akmaev, F. Wu, T.-W. Fang, M. Iredell, and A. Richmond (2011), Forecasting the dynamic and electrodynamic response to the January 2009 sudden stratospheric warming, *Geophys. Res. Lett.*, *38*, L13102, doi:10.1029/2011GL047732.
Goncharenko, L., and S.-R. Zhang (2008), Ionospheric signatures of sudden stratospheric warming: Ion temperature at middle latitude, *Geophys. Res. Lett.*, *35*, L21103, doi:10.1029/2008GL035684.
Goncharenko, L. P., A. J. Coster, J. L. Chau, and C. E. Valladares (2010a), Impact of sudden stratospheric warmings on equatorial ionization anomaly, *J. Geophys. Res.*, *115*, A00G07, doi:10.1029/2010JA015400.
Goncharenko, L. P., J. L. Chau, H.-L. Liu, and A. J. Coster (2010b), Unexpected connections between the stratosphere and ionosphere, *Geophys. Res. Lett.*, *37*, L10101, doi:10.1029/2010GL043125.
Goncharenko, L. P., A. J. Coster, R. A. Plumb, and D. I. V. Domeisen (2012), The potential role of stratospheric ozone in the stratosphere-ionosphere coupling during stratospheric warmings, *Geophys. Res. Lett.*, *39*, L08101, doi:10.1029/2012GL051261.
Goncharenko, L. P., V. W. Hsu, C. G. M. Brum, S.-R. Zhang, and J. T. Fentzke (2013), Wave signatures in the midlatitude ionosphere during a sudden stratospheric warming of January 2010, *J. Geophys. Res. Space Physics*, *118*, 472–487, doi:10.1029/2012JA018251.
Gong, Y., Q. Zhou, and S. Zhang (2013), Atmospheric tides in the low-latitude E and F regions and their responses to a sudden stratospheric warming event in January 2010, *J. Geophys. Res. Space Physics*, *118*, 7913–7927, doi:10.1002/2013JA019248.
Hagan, M. E., and J. M. Forbes (2002), Migrating and nonmigrating diurnal tides in the middle and upper atmosphere excited by tropospheric latent heat release, *J. Geophys. Res.*, *107*(D24), 4754, doi:10.1029/2001JD001236.
Hagan, M. E., and J. M. Forbes (2003), Migrating and nonmigrating semidiurnal tides in the upper atmosphere excited by tropospheric latent heat release, *J. Geophys. Res.*, *108*(A2), 1062, doi:10.1029/2002JA009466.
Harvey, V. L., R. B. Pierce, and M. H. Hitchman (2002), A climatology of stratospheric polar vortices and anticycles, *J. Geophys. Res.*, *107*(D20), 4442, doi:10.1029/2001JD001471.
Hoffmann, P., W. Singer, D. Keuer, W. K. Hocking, M. Kunze, and Y. Murayama (2007), Latitudinal and longitudinal variability of mesospheric winds and temperatures during stratospheric warming events, *J. Atmos. Sol. Terr. Phys.*, *69*, 2355–2366.
Jin, H., Y. Miyoshi, D. Pancheva, P. Mukhtarov, H. Fujiwara, and H. Shinagawa (2012), Response of migrating tides to the stratospheric sudden warming in 2009 and their effects on the ionosphere studied by a whole atmosphere-ionosphere model GAIA with COSMIC and TIMED/SABER observations, *J. Geophys. Res.*, *117*, A10323, doi:10.1029/2012JA017650.
Kudeki, E., S. Bhattacharyya, and R. F. Woodman (1999), A new approach in incoherent scatter F region ExB drift measurements at Jicamarca, *J. Geophys. Res.*, *104*, 28,145–28,162.
Lei, J., W. Wang, A. G. Burns, S. C. Solomon, A. D. Richmond, M. Wiltberger, L. P. Goncharenko, A. Coster, and B. W. Reinisch (2008), Observations and simulations of the ionospheric and thermospheric response to the December 2006 geomagnetic storm: Initial phase, *J. Geophys. Res.*, *113*, A01314, doi:10.1029/2007JA012807.
Limpasuvan, V., D. W. Thompson, and D. L. Hartmann (2004), The life cycle of the Northern Hemisphere sudden stratospheric warmings, *J. Clim.*, *17*, 2584–2596.
Lin, C. H., J. T. Lin, L. C. Chang, J. Y. Liu, C. H. Chen, W. H. Chen, H. H. Huang, and C. H. Liu (2012), Observations of global ionospheric responses to the 2009 stratospheric sudden warming event by FORMOSAT-3/COSMIC, *J. Geophys. Res.*, *117*, A06323, doi:10.1029/2011JA017230.
Liu, H.-L., and A. D. Richmond (2013), Attribution of ionospheric vertical plasma drift perturbations to large-scale waves and the dependence on solar activity, *J. Geophys. Res. Space Physics*, *118*, 2452–2465, doi:10.1002/jgra.50265.
Liu, H.-L., and R. G. Roble (2002), A study of a self-generated stratospheric sudden warming and its mesospheric-lower thermospheric impacts using the coupled TIME-GCM/CCM3, *J. Geophys. Res.*, *107*(D23), 4695, doi:10.1029/2001JD001533.
Liu, H.-L., W. Wang, A. D. Richmond, and R. G. Roble (2010), Ionospheric variability due to planetary waves and tides for solar minimum conditions, *J. Geophys. Res.*, *115*, A00G01, doi:10.1029/2009JA015188.
Manney, G. L., et al. (2008), The evolution of the stratopause during the 2006 major warming: Satellite data and assimilated meteorological analyses, *J. Geophys. Res.*, *113*, D11115, doi:10.1029/2007JD009097.
Manney, G. L., M. J. Schwartz, K. Krüger, M. L. Santee, S. Pawson, J. N. Lee, W. H. Daffer, R. A. Fuller, and N. J. Livesey (2009), Aura Microwave Limb Sounder observations of dynamics and transport during the record-breaking 2009 Arctic stratospheric major warming, *Geophys. Res. Lett.*, *36*, L12815, doi:10.1029/2009GL038586.
Millward, G. H., I. C. F. Muller-Wodarg, A. D. Aylward, T. J. Fuller-Rowell, A. D. Richmond, and R. J. Moffett (2001), An investigation into the influence of tidal forcing on F region equatorial vertical ion drift using a global ionosphere-thermosphere model with coupled electrodynamics, *J. Geophys. Res.*, *106*(A11), 24,733–24,744, doi:10.1029/2000JA000342.
Pancheva, D., and P. Mukhtarov (2011), Stratospheric warmings: The atmosphere-ionosphere coupling paradigm, *J. Atmos. Sol. Terr. Phys.*, *73*(13), 1697–1702.
Pedatella, N. M., and J. M. Forbes (2010), Evidence for stratosphere sudden warming-ionosphere coupling due to vertically propagating tides, *Geophys. Res. Lett.*, *37*, L11104, doi:10.1029/2010GL043560.
Pedatella, N. M., and H.-L. Liu (2013), The influence of atmospheric tide and planetary wave variability during sudden stratosphere warmings on the low latitude ionosphere, *J. Geophys. Res. Space Physics*, *118*, 5333–5347, doi:10.1002/jgra.50492.
Pedatella, N. M., H.-L. Liu, A. D. Richmond, A. Maute, and T.-W. Fang (2012), Simulations of solar and lunar tidal variability in the mesosphere and lower thermosphere during sudden stratosphere warmings and their influence on the low-latitude ionosphere, *J. Geophys. Res.*, *117*, A08326, doi:10.1029/2012JA017858.
Pedatella, N. M., et al. (2014), The neutral dynamics during the 2009 sudden stratosphere warming simulated by different whole atmosphere models, *J. Geophys. Res. Space Physics*, *119*, 1306–1324, doi:10.1002/2013JA019421.
Rishbeth, H. (1962), Atmospheric composition and the F layer of the ionosphere, *Planet. Space Sci.*, *9*, 149–152.
Rishbeth, H. (1967), The effect of winds on the ionospheric F2-peak, *J. Atmos. Sol. Terr. Phys.*, *29*, 225–238.

Roble, R. G. (1995), Energetics of the mesosphere and thermosphere, in *The Upper Mesosphere and Lower Thermosphere: A Review of Experiment and Theory, Geophys. Monogr. Ser.*, vol. 87, edited by R. M. Johnson and T. L. Killeen, pp. 1–21, AGU, Washington, D. C., doi:10.1029/GM087p0001.

Roble, R. G., and E. C. Ridley (1994), A thermosphere-ionosphere-mesosphere-electrodynamics general circulation model (TIME-GCM): Equinox solar cycle minimum simulations (30–500 km), *Geophys. Res. Lett.*, *21*, 417–420.

Rocken, C., Y.-H. Kuo, W. Schreiner, D. Hunt, S. Sokolovskiy, and C. McCormick (2000), COSMIC system description, *Terr. Atmos. Oceanic Sci.*, *11*(1), 21–52.

Rodrigues, F. S., G. Crowley, S. M. I. Azeem, and R. A. Heelis (2011), C/NOFS observations of the equatorial ionospheric electric field response to the 2009 major sudden stratospheric warming event, *J. Geophys. Res.*, *116*, A09316, doi:10.1029/2011JA016660.

Sassi, F., H.-L. Liu, J. Ma, and R. R. Garcia (2013), The lower thermosphere during the Northern Hemisphere winter of 2009: A modeling study using high-altitude data assimilation products in WACCM-X, *J. Geophys. Res. Atmos.*, *118*, 8954–8968, doi:10.1002/jgrd.50632.

Sathishkumar, S., and S. Sridharan (2013), Lunar and solar tidal variablities in mesospheric winds and EEJ strength over Tirunelveli (8.7°N, 77.8°E) during the 2009 major stratospheric warming, *118*, *533–541*, doi:10.1029/2012JA018236.

Scherliess, L., and B. G. Fejer (1999), Radar and satellite global equatorial F region vertical drift model, *J. Geophys. Res.*, *104*(A4), 6829–6842, doi:10.1029/1999JA900025.

Schoeberl, M. R. (1978), Stratospheric warmings: Observations and theory, *Rev. Geophys.*, *16*(4), 521–538, doi:10.1029/RG016i004p00521.

Schreiner, W. S., S. V. Sokolovskiy, C. Rocken, and D. C. Hunt (1999), Analysis and validation of GPS/MET radio occultation data in the ionosphere, *Radio Sci.*, *34*(4), 949–966.

Siskind, D. E., D. P. Drob, K. F. Dymond, and J. P. McCormack (2014), Simulations of the effects of vertical transport on the thermosphere and ionosphere using two coupled models, *J. Geophys. Res. Space Physics*, *119*, 1172–1185, doi:10.1002/2013JA019116.

Smith, A. K., M. Lopez-Puertas, M. Garcia-Comas, and S. Tukiainen (2009), SABER observations of mesospheric ozone during NH late winter 2002–2009, *Geophys. Res. Lett.*, *36*, L23804, doi:10.1029/2009GL040942.

Stening, R. J. (1977), Electron density profile changes associated with the equatorial electrojet, *J. Atmos. Terr. Phys.*, *39*, 157–164.

Stening, R. J., C. E. Meek, and A. H. Manson (1996), Upper atmosphere wind systems during reverse equatorial electrojet events, *Geophys. Res. Lett.*, *23*(22), 3243–3246.

Stening, R. J., J. M. Forbes, M. E. Hagan, and A. D. Richmond (1997), Experiments with a lunar atmospheric tidal model, *J. Geophys. Res.*, *102*(D12), 13,465–13,471, doi:10.1029/97JD00778.

Walterscheid, R. K., G. G. Sivjee, and R. G. Roble (2000), Mesospheric and lower thermosphere manifestations of a stratospheric warming event over Eureka Canada (80°N), *Geophys. Res. Lett.*, *27*, 2897–2900.

Yamazaki, Y., and A. D. Richmond (2013), A theory of ionospheric response to upward-propagating tides: Electrodynamic effects and tidal mixing effects, *J. Geophys. Res. Space Physics*, *118*, 5891–5905, doi:10.1002/jgra.50487.

Yamazaki, Y., K. Yumoto, D. J. McNamara, T. Hirooka, T. Uozumi, K. Kitamura, S. Abe, and A. Ikeda (2012a), Ionospheric current system during sudden stratospheric warming events, *J. Geophys. Res.*, *117*, A03334, doi:10.1029/2011JA017453.

Yamazaki, Y., A. D. Richmond, and K. Yumoto (2012b), Stratospheric warmings and the geomagnetic lunar tide: 1958–2007, *J. Geophys. Res.*, *117*, A04301, doi:10.1029/2012JA017514.

Yue, X., W. S. Schreiner, J. Lei, C. Rocken, D. C. Hunt, Y.-H. Kuo, and W. Wan (2010), Global ionospheric response observed by COSMIC satellites during the January 2009 stratospheric sudden warming event, *J. Geophys. Res.*, *115*, A00G09, doi:10.1029/2010JA015466.